Demonstration of an Anterior Diffusional Pathway for Solutes in the Normal Human Eye with High Spatial Resolution Contrast-Enhanced Dynamic MR Imaging

Robert J. Bert,[1] Shelton D. Caruthers,[2] Hernan Jara,[3] Jaroslaw Krejza,[4,5] Elias R. Melhem,[4] Nancy H. Kolodny,[6] Samuel Patz,[7] and Thomas F. Freddo[8]

Purpose. The present studies were conducted to determine whether a diffusional pathway for solutes exists from the ciliary body stroma to the anterior chamber of the human eye. The existence of such a pathway has been demonstrated in rabbits and monkeys, but such a pathway in humans would necessitate a shift in the physiological paradigm of the blood–aqueous barrier.

Methods. Seven normal human volunteers (five men, two women; age range, 27 to 59 years) underwent nine dynamic T1-weighted, spin-echo MR imaging studies, using intravenous, gadolinium-based contrast agents.

Results. In all cases, signal intensity rose rapidly in the ciliary body. In all subjects, there was a measurable latent rise in signal strength (enhancement) in the anterior chamber. Signal enhancement typically occurred in the angle of the anterior chamber earlier, and to a greater degree, than within the center of the chamber. Increased signal within the posterior chamber was significantly less than in the anterior chamber, with measured increases probably attributable to volume averaging.

Conclusions. These findings are consistent with the existence of an anterior diffusional pathway in the human eye. The model warrants further testing. (*Invest Ophthalmol Vis Sci.* 2006;47:5153–5162) DOI:10.1167/iovs.05-0372

From the [1]Department of Radiology, Health Sciences Center, University of Colorado, Denver, Colorado; [2]Philips Medical Systems, MRI, St. Louis, Missouri; the Departments of [3]Radiology and [8]Ophthalmology and Pathology, Boston Medical Center, Boston, Massachusetts; the [4]Department of Radiology, University of Pennsylvania Medical Center, Philadelphia, Pennsylvania; the [5]Department of Radiology, Gdansk Medical Academy, Gdansk, Poland; the [6]Department of Chemistry, Wellesley College, Wellesley, Massachusetts; and [7]Tufts-New England Medical Center, Boston, Massachusetts.

Supported by National Eye Institute Grant EY-13825 (TFF) and by unrestricted grants to the Department of Ophthalmology at Boston University from Research to Prevent Blindness, Inc. and The Massachusetts Lions Eye Research Fund, Inc.

Submitted for publication March 23, 2005; revised August 28, and December 4, 2005; accepted October 5, 2006.

Disclosure: **R.J. Bert,** None; **S.D. Caruthers,** Philips Medical Systems (E); **H. Jara,** None; **J. Krejza,** None; **E.R. Melhem,** None; **N.H. Kolodny,** None; **S. Patz,** None; **T.F. Freddo,** None

The publication costs of this article were defrayed in part by page charge payment. This article must therefore be marked "*advertisement*" in accordance with 18 U.S.C. §1734 solely to indicate this fact.

Corresponding author: Robert J. Bert, Department of Radiology, University of Colorado, Denver Health Sciences Center, 4200 E. Ninth Avenue, A034, Denver, CO 80262; robert.bert@uchsc.edu.

The presence of a blood–aqueous barrier in the normal mammalian eye is well established.[1] The source of the small amount of plasma-derived protein that enters the normal aqueous humor, however, has been uncertain. Previous studies in rabbits[2] and monkeys,[3] in which correlative fluorophotometric and morphologic methods were used, first demonstrated the existence of a diffusional pathway for plasma-derived solutes from the ciliary body stroma, directly into the anterior chamber, via the root of the iris.[4] Extensive computational modeling has suggested that most of the plasma-derived protein in the normal aqueous humor enters the aqueous by this pathway, bypassing the posterior chamber.[2,3]

In vivo confirmation of this pathway has been demonstrated, in these same species, with a 4.7-T, 30-cm bore magnetic resonance imaging (MRI) system, after intravenous injection of the contrast agent, gadopentetate dimeglumine (Magnevist; Berlex, Wayne, NJ).[5] Several aspects of aqueous humor dynamics distinguish the human eye from all other species. One major example is that in all species, except humans, there is a volume-dependent increase in outflow facility, when the anterior chamber is perfused.[6] Therefore, the presence of an anterior pathway in rabbits and monkeys does not mean that such a pathway exists in humans.

The demonstration that this pathway was traceable and quantifiable using MRI presented the opportunity to examine directly whether this same pathway exists in the normal human eye. The goal of our present study was to test the hypothesis that an anterior diffusional pathway also exists in the normal human eye.

Methods

Subject Enlistment

These IRB-approved studies were in compliance with the tenets of the Declaration of Helsinki. Informed consent was obtained from the subjects after explanation of the nature and possible consequences of the study. All subjects were initially screened for prior occupational or environmental metal fragment exposure, previous eye surgery, eye and visual pathway diseases, the presence of pacemakers or other in situ electronic devices, and claustrophobia. After this initial screening process, all volunteers underwent complete eye examinations. Ten volunteers were screened for the study. Of those, three subjects were eliminated: one because of previous eye surgery (radial keratotomy), one because of claustrophobia, and one because of minimal contrast extravasation before beginning the study, without further sequela. Seven normal volunteers completed the study (five men and two women; age range, 27 to 59 years). Two subjects were examined with both an ionic contrast agent and a nonionic contrast agent. A single

individual was examined twice with the same contrast material, to examine repeatability of the measurements.

Subject Preparation

Subjects were typically examined in the early morning, after overnight fasting, to avoid diurnal variations in aqueous dynamics. The subjects were prepared in a manner previously described.[7] In brief, images were obtained from a single eye, taped shut, using a flexible circular surface coil (8-cm inner diameter [ID], 14 cm [OD]; Philips Medical Systems, Shelton CT). In addition, it is well known that the MRI signal is influenced by air–tissue interfaces. This is because the difference in magnetic susceptibility at these interfaces creates a local magnetic field inhomogeneity that can dephase (or attenuate) the MRI signal. Magnetic susceptibility defines the magnetization response per unit field strength of a material. To reduce this effect, a moistened cellulose pad was taped in place over the study eye, to move this interface farther away from the eyelid. A second dry pad provided a cushion between the eyelid and surface coil, improving patient comfort and stabilizing the taped eyelid. The subjects were instructed to fixate the contralateral open eye on a crossbar target during image acquisition. This method had the positive effect of reducing motion artifact in the images to a minimum. The open eye was allowed to blink physiologically, which avoided any drying and abrasion risk during the study. The dynamic imaging sequences used one of two gadolinium contrast agents: gadopentetate dimeglumine (MW 938, 469 mg/mL, 0.4 mL/kg body weight; Magnevist; Berlex) or gadoteridol (MW 558.7, 279.3 mg/mL, 0.4 mL/kg body weight; ProHance; Bracco Diagnostics, Princeton, NJ).

Imaging Parameters

MR imaging was performed with a 1.5-Tesla superconducting system (Gyroscan ACS-NT PowerTrak 6000; Philips Medical Systems). Signal intensity (SI) measurements were performed with a dedicated image processing workstation (EasyVision CT/MR, software release 2; Philips Medical Systems). Typical imaging parameters used for the T_1-weighted conventional spin–echo pulse sequence were TR = 400 ms, TE = 17 ms, four slices, NSA (number of signal averages) = 6, voxel dimensions = $0.21 \times 0.21 \times 2$ mm^3, and field of view (FOV) = 4 to 5 cm. A reduced-phase FOV of 65% was used, with partial zero filling (phase % = 65). Each dynamic scan was ~4 minutes, 48 seconds long. The image data were reconstructed in a 512×512 matrix, with zero filling.

Data Acquisition

Compressed foam was used to constrain the subject's head, to minimize motion artifacts, and baseline images were acquired. Immediately after antecubital injection of the Gd-based contrast agent, defined as $t = 0$, the same image data set was then reacquired. Additional data sets were acquired at 10-minute intervals, for 90 minutes or until the volunteer ended the examination (earliest termination, 60 minutes). The following structures were analyzed: the study regions (anterior chamber, posterior chamber, and ciliary body), two negative controls (lens and vitreous humor), and two positive controls (extraocular muscles and chorioretina). Rarely, individual images were blurred, making them inadequate for analysis, as assessed by the neuroradiologist (RJB). In these cases, extra images were immediately acquired and the time of imaging recorded.

Data Analysis

A commercial statistics package (Excel; Microsoft Corp., Redmond, WA) was used for numerical analysis. The most central images from the sets, with least evidence of motion artifact, were quantitatively evaluated in the following manner.

Region of Interest Measurement. The region of interest (ROI) measurements were performed with image-analysis software available on the imaging workstation (EasyVision CT/MR, software ver. 2; Philips Medical Systems), ROIs (Fig. 1) were drawn by hand. Care was taken to obtain the largest possible areas, while avoiding edges with adjacent structures, to avoid voxels that straddle a tissue interface and therefore do not fully represent the structure being measured. ROIs had to be drawn by hand and not automatically transferred to each new image, due to slight movements of the head or eye between image acquisitions. Mean signal amplitude in arbitrary units $\hat{S}$, SD (σ), and number of voxels within ROIs in the different eye tissues and compartments were measured, as well as the mean and SD of pixels in a "tissue-free" or background region. These latter values were used to estimate system noise (N_{sys}). The underlying noise distribution in the raw data is known to be Gaussian and position-independent in the absence of artifactual sources.[8] Image reconstruction and system noise analysis are detailed further in the Appendix (System Noise Analysis section).

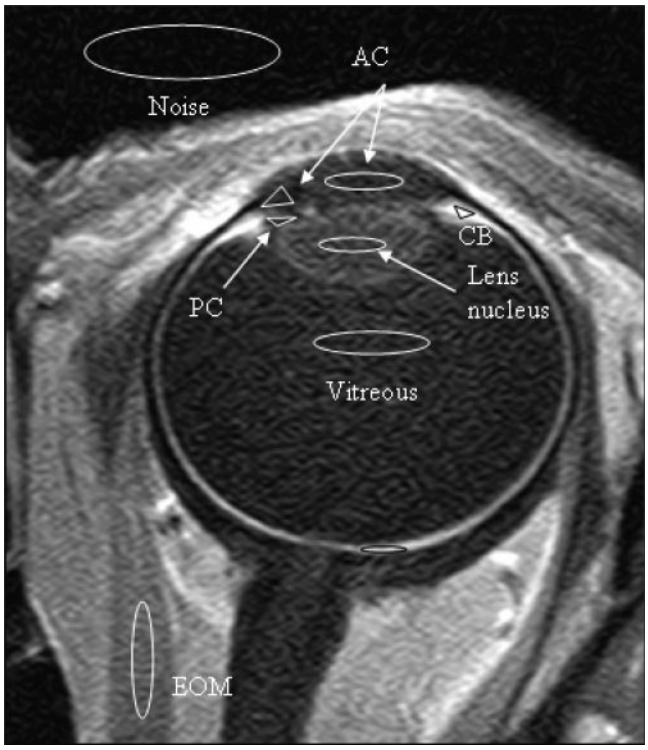

FIGURE 1. Regions of interest (ROI) defined for measuring mean voxel contrast. AC, anterior chamber; PC, posterior chamber; CB, ciliary body; EOM, muscles.

Autoscaling Corrections. After the original data were acquired, we discovered that the scanner had rescaled the data at each time point using internal algorithms (see Appendix) that are designed to keep measured signal relatively constant. If left uncorrected, this autoscaling would confound the results. To correct for autoscaling, we also present data with a correction factor derived from the nonenhancing vitreous humor signal, which should not change over the course of a study. That is, we exploited the known absence of vitreous enhancement to create a correction factor that keeps the time-dependent mean ROI vitreous signal constant and then applied this correction to all the data. (See Autoscaling in the Appendix for details). Parameters for each subject are listed in Table 1.

Quantitative Measures of the Change in Signal from Baseline. For each structure and at each measured time point t, the change in the mean ROI signal or contrast, *$\hat{C}(t)$, as well as the contrast-to-noise ratio,* $\hat{C}(t)/N_{sys}(t)$, were calculated relative to values obtained from the $t = 0$ baseline, nonenhanced images, by using the formulas identified in Contrast-to-Noise Calculations in the Appendix.

TABLE 1. Correction Equation and Individual Subject Parameters Based on the Vitreous Data Fit for Each Subject

Subject	$\Delta\hat{S}$ Signal Amplitude (Arbitrary Units)	*M* Signal Amplitude/ Unit Time	*B* Signal Amplitude (Arbitrary Units)
1	66	−0.2	346
2	69	0.42	385
3	74	−0.035	406
4	33	−0.7	422
5	39	−0.2	405
6	41	−0.8	310
7	20	−2	412
8	58	−0.19	396

Correction function: for $t = 0$: $\hat{S}_{sc}(0) = \hat{S}_{sm}(0)$; for $t > 0$: $\hat{S}_{sc}(t) = \hat{S}_{sm}(t) + (\hat{S}_{sm}(0)/\hat{S}_{vm}(0))(\Delta\hat{S} - M \times t)$, where $\Delta\hat{S} = (\hat{S}_{vm}(0) - B)$. $\hat{S}(0)$, mean ROI signal amplitude from a structure at baseline (nonenhanced); $\hat{S}(t)$, mean signal within an ROI at time (*t*) after contrast administration; c, m, designate corrected and measured values; *t,* time in minutes since administration of contrast; $\Delta\hat{S}$, value of applied step function; *S, v,* designate structure of interest and the vitreous humor; *B,* back projected intercept predicted by the linear least squares fit of vitreous data points of the $\hat{S}_v(t)$ curve calculated from *t,* 4 minutes to last postcontrast data point; *M,* slope from the same curve fit.

Data Presentation

For each analyzed structure, plots are presented as a function of time for the measured mean signal $\hat{S}_m(t)$, the corrected (or adjusted) mean signal $\hat{S}_c(t)$, the normalized corrected (or adjusted) mean signal and the corrected (or adjusted) contrast to noise $\hat{C}_c(t)/N_c(t)$. The adjusted data sets, $\hat{S}_c(t)$, were fit with curves by means of linear and nonlinear least squares techniques, using curve-fitting routines within the statistical program (Excel; Microsoft Corp.). The selection of the mathematical equations used to fit each data set was based on both visual inspection of the time-dependent form of the data and trial and error (augmented by comparing the least cumulative squared error for different trials). Curve formulas, parameters, and the mean squared and RMS errors for the fitted curves are given in Table 2.

A summary of the fits to the adjusted data is described here. Details are in the Appendix. Linear curve fits (i.e., where the slope and intercept were fit parameters) were determined for the vitreous humor and posterior chamber. The ciliary body and extraocular muscles demonstrated very rapid rising phases that were beyond our technique's ability to time-resolve the rising phase. However, a declining phase was identifiable and was fit by a single exponential function, by using the least-squares method.

Nonlinear curves were fit to anterior chamber data using the software's "solver function" tool, which minimized the sum of the squares of the error by adjusting the fit parameters of several test equations. Visual inspection of the data suggested that the data might be well fit by the logistic curve (see Appendix for details) or variable transforms of exponentials (e.g., $A_0(1 - e^{-kt})$, where A_0 and k are fitted parameters). The logistic curve fit provided less total error (cumulative squares of the errors) than different exponential forms that we tested.

The anterior chamber data appeared to contain a latency period before measurable enhancement. This latency was estimated both visually and by testing cumulative squared error values in the curve-fitting program. The latency that provided the least sum of the squared error for the logistic curve fit was chosen.

Intersubject Comparison

Composite, time-dependent plots of $\hat{S}_m(t)$, $\hat{S}_c(t)$ and $\hat{C}_c(t)/N_c(t)$ for values of the mean anterior chamber central, anterior chamber angle, posterior chamber, and ciliary body were prepared in the following manner: $\hat{S}_m(t)$, $\hat{S}_c(t)$, and $\hat{C}_c(t)/N_c(t)$ at each time point, from a given structure, were averaged across subjects at each time point and plotted as composite, time-depended curves.

The Wilcoxon paired test was used to compute probabilities for comparison of the maximum (with reference to time) average contrast enhancement observed for each structure in both the unadjusted and adjusted composite data sets. Because of time constraints, one subject could only participate in the study for a total of 60 minutes. This limited the intersubject comparisons to this allotted time.

RESULTS

In all subjects who completed the MRI examination, initial non–contrast-enhanced images were of sufficient spatial resolution and quality to differentiate the structures in question—namely, the anterior chamber, the iris, the ciliary body, and the posterior chamber, as judged by the neuroradiology specialist (RJB) and eye pathologist (TFF). The imaging technique, using a single closed eye with overlying cellulose pads, helped in reducing motion and susceptibility artifacts and lead to good quality, high-spatial resolution images. The precontrast anterior chamber and the vitreous humor showed no statistically significant MR signal differences within any subject.

Subjectively, in all subjects completing the study, there was immediate enhancement of the chorioretina and ciliary body after gadolinium administration, demonstrating appropriate levels of intravenous contrast. The anterior chamber enhanced slowly, after an initial delay of several minutes, beginning from its periphery and gradually filling the central anterior chamber (complete time course not shown). The vitreous and lens nucleus did not enhance at any time. The central posterior chamber did not appear to enhance either. A modest increased signal that was stable over time was noted in the margins of the posterior chamber. This signal appeared to reflect motion blurring and/or the partial volume effects of the enhancing

TABLE 2. Formulas, Parameter Values, Mean Squared Error, and Root Mean Squared Error for the Curves Fitted in Figure 3

	Formula	Latency	Slope	$\frac{S_i}{S_m}$	Σ Error^2	RMS
ACA	$S_i = 1/3(S(0) + S(4))$	4 minutes	$k = 0.037$	625	6960	83.4
	$\hat{S}(t) = S_iS_m/(S_i + (S_m - S_i)(e^{-kt}))$			1073		
ACC	$S_i = 1/3(S(0) + S(4) + S(14))$	14 minutes	$k = 0.031$	619	1894	43.5
	$\hat{S}(t) = S_iS_m/(S_i + (S_m - S_i)(e^{-kt}))$			1085		
PC	$\hat{S}(t) = M \times t + S_i$	None	$M = 0.39$	629	20630	144
Vit	$\hat{S}(t) = M \times t + S_i$	None	$M = 0$	479	1649	40.6
CB	$\hat{S}(t) = S_ie^{-kt}$	Not measurable	$k = 0.0023$	2163	99100	315
EOM	$\hat{S}(t) = S_ie^{-kt}$	Not measurable	$k = 0.0031$	1074.5	28590	169

Σ error^2 = sum squared error. RMS = root squared error or $(\Sigma \text{ error}^2)^{1/2}$. ACA, anterior chamber angle; ACC, anterior chamber center; PC, posterior chamber; Vit, vitreous humor; CB, ciliary body; EOM, extraocular muscles; S_i, calculated initial value of adjusted mean ROI signal amplitude; S_m, equilibrium value of adjusted mean ROI signal amplitude; $\hat{S}(t)$: mean ROI signal amplitude at time *t.* $\hat{S}(0)$, $\hat{S}(4)$, $\hat{S}(14)$, adjusted measured mean ROI signal amplitude at times 0, 4 and 14 minutes; *M,* slope of linear fit; *k,* fitted exponential parameter (analog of slope in linear equations); *t,* time in minutes post contrast injection.

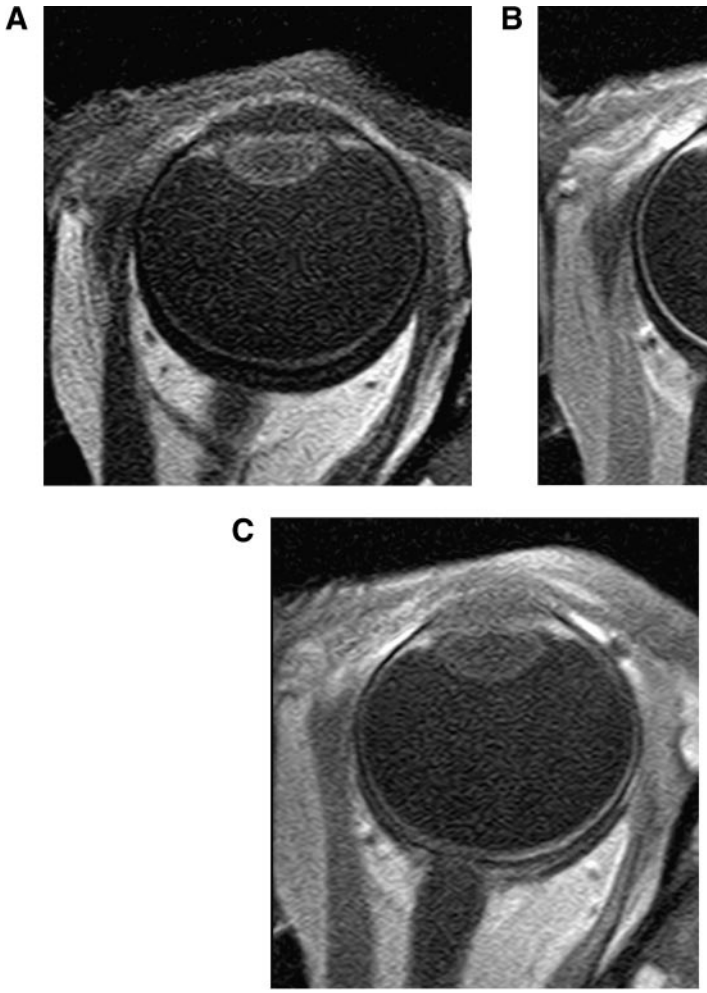

FIGURE 2. (**A**) Precontrast; (**B**) immediate postcontrast; and (**C**) delayed post contrast images from a typical study.

ciliary body voxels at the edges of the posterior chamber. For one subject, Figure 2 shows precontrast, immediately postcontrast, and late postcontrast images. Figure 3 shows typical graphs, from the same subject, of the time-resolved mean ROI signal amplitude of the central anterior chamber, peripheral anterior chamber, posterior chamber, vitreous, ciliary body, and extraocular muscles (Figs. 3A: measured data; 3B: adjusted values; 3C: normalized adjusted values; and 3D: adjusted contrast/noise). Table 1 gives the correction equation, and individual subject parameters based on the vitreous data fit, for each subject. Thus, in the adjusted vitreous, data points were not exactly constant, because the correction that is applied uses the fit to the vitreous data rather than each corresponding vitreous data point. Thus, as an example, in Figure 3C, the normalized vitreous signal at each time point is not exactly equal to one. Rather, the plotted data show the deviation between the fitted curve and the normalized measured points.

Figure 4 shows the adjusted data with least-squares fitting of chosen curves to the data (see methods, data analysis). Linear fits were applied to the vitreous and posterior chamber. Data acquisition was insufficiently rapid to define the rise portion of the EOM and CB data. However, the decaying portions of these data were fit by first-order exponential decay. Logistic curves were fit to the peripheral and central anterior chamber data (see the Methods section).

The anterior chamber angle and center began detectable enhancing after latencies of ~4 and 14 minutes in this example subject, estimated visually and empirically (range over subjects for anterior angle center: 12.5–30.5 minutes; see the Methods section), reaching a peak ~74 minutes after injection. The estimation of the latency was made both visually and by trial and error, and these results bear similarities to the results obtained in animals.[5]

Table 2 gives the formulas, parameter values, cumulative squared error, and root mean squared error for the curves fitted in Figure 4.

Figure 5A is a scatterplot of the averaged across-subject (all examinations) unadjusted raw data, showing average ROI signal amplitudes versus time. Figure 5B is a similar plot of the adjusted across-subject data. Figure 5C shows the across-subject averaged adjusted contrast-to-noise ratio.

Table 3 shows the probabilities calculated by the Wilcoxon paired tests for comparisons of maximum enhancement, within 60 minutes, between the anterior chamber angle, ante-

FIGURE 3. (**A**) Scatterplot with SE bars for regions of interest of several anatomic structures in a typical human eye. (**B**) Scatterplot similar to (**A**), with adjusted mean ROI signal amplitudes (see the Appendix). (**C**) Scatterplot of the normalized, adjusted data, where the adjusted signal at each time point is divided by the initial, precontrast signal. (**D**) Scatterplot showing adjusted contrast-to-noise (C/N_s) ratios for each of the same structures in (**A–C**). AC ang, anterior chamber angle; AC Cen, anterior chamber center; PC, posterior chamber; EOM, extraocular muscles; Vitr, vitreous humor; CB, ciliary body.

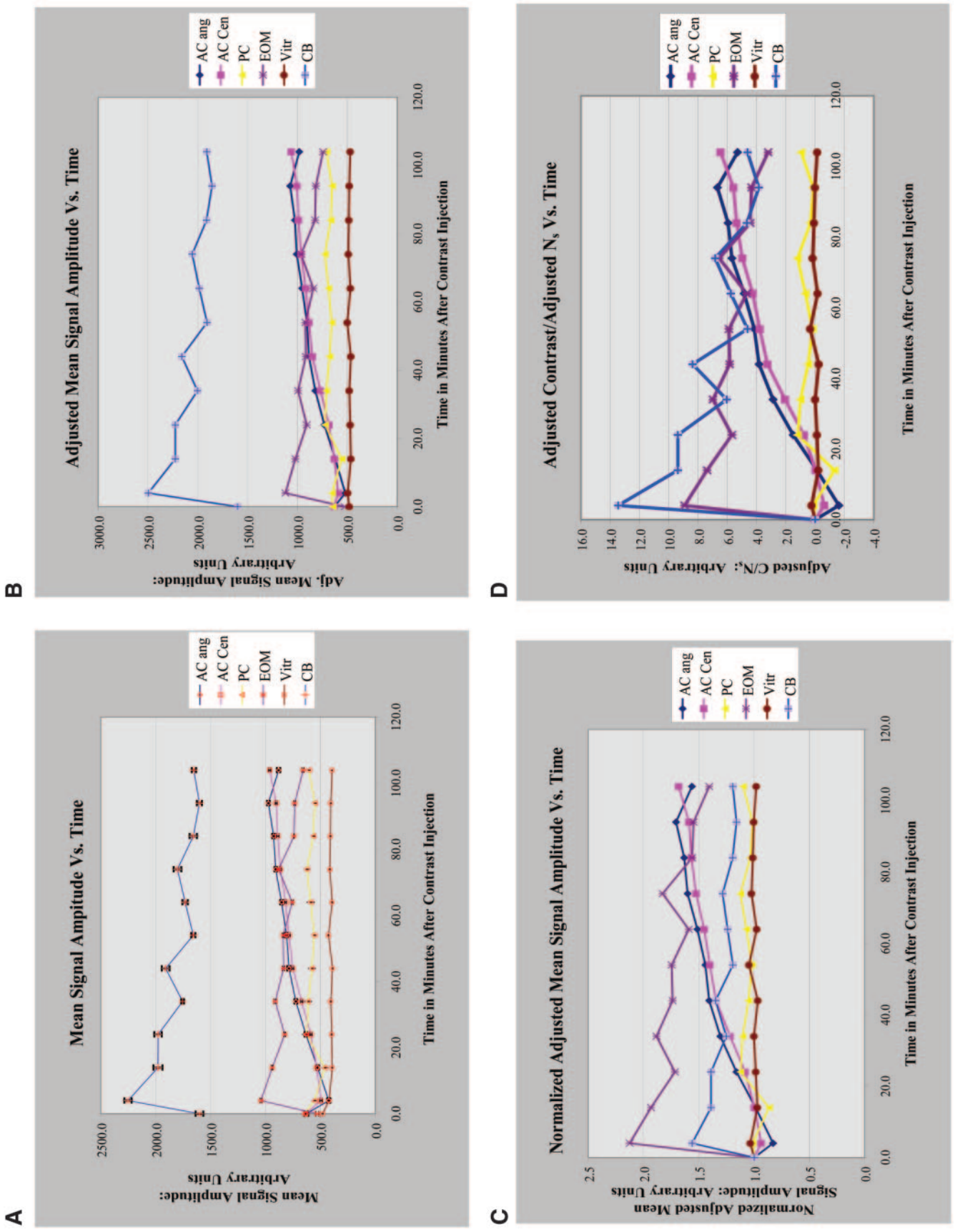

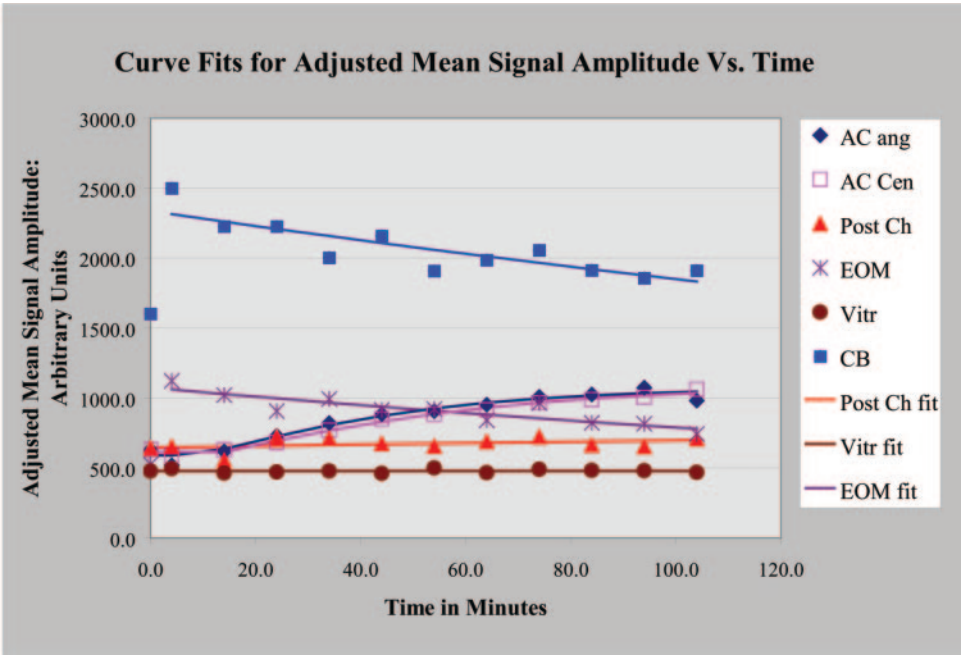

FIGURE 4. Scatterplots of adjusted data with linear and nonlinear least squares fit curves. AC ang, anterior chamber angle; AC Cen, anterior chamber center; Post Ch, posterior chamber; EOM, extraocular muscles; Vitr, vitreous humor; CB, ciliary body; Post Ch fit, linear least-squares fit to posterior chamber data; Vitr fit, linear least-squares fit to vitreous data; EOM fit, exponential least squares fit to declining phase of extraocular muscle data; CB fit, exponential least-squares fit to declining phase of ciliary body data; AC Ang fit, least-squares logistic curve fit to anterior chamber angle; AC Cen fit, least-squares logistic curve fit to anterior chamber center.

rior chamber center, posterior chamber, and ciliary body and the vitreous and noise data. Also compared are probabilities of the anterior chamber angle, anterior angle center, and posterior chamber. Enhancement was significant for the ciliary body, anterior chamber (at both its angle and center), and posterior chamber versus the vitreous. However, there was significantly greater enhancement of the anterior chamber angle versus the anterior chamber center (Wilcoxon paired test, $P \leq 0.05$, not shown in the table) and significantly greater enhancement of the anterior chamber center versus the posterior chamber.

DISCUSSION

Our results showed rapid enhancement of the ciliary body and a gradual enhancement of the anterior chamber in all cases. Most subjects demonstrated relatively stable, minimal enhancement of the posterior chamber, which was statistically less than both the center and angle of the anterior chamber. Furthermore, enhancement in the anterior chamber angle was significantly greater than in the center of the anterior chamber. This demonstrates signal enhancement that is highest at the anterior chamber angle and lowest in the posterior chamber. Such a gradient is opposite that expected if the dominant pathway of entrance was leakage into the posterior chamber, followed by entry into the anterior chamber by bulk flow.

The minimal enhancement of the posterior chamber appeared to result from edge effects, volume averaging and motion blurring (see the Methods section). With the resolution limitations of current imaging methods, it seems inevitable that there is some contamination of the measurement of the small volume in the posterior chamber, with the adjacent, avidly enhancing ciliary body and iris. Our findings are similar to those in prior reports in rabbit and monkey eyes: Aqueous enhancement is first apparent near the iris root. Consistent with prior reports involving the use fluorophors,[2,3] the contrast was picked up by the convectional flow of aqueous, enhancing first the periphery of the anterior chamber and gradually mixing toward the center (complete time course not shown).

The stability of the minimal enhancement in the posterior chamber reinforces the role of bulk flow of aqueous forward through the pupil, as an important factor limiting back-diffusion of solutes delivered to the anterior chamber via this anterior pathway. This element and the demonstrated presence of tight junctions between the posterior epithelial cells of the iris[9] are underappreciated but essential components of the blood–aqueous barrier.

Overall, our results support the existence of a pathway for diffusion of plasma-derived solutes into the anterior chamber of the human eye, similar to that previously demonstrated in rabbits and monkeys.[2,3,5] Combined with a predominantly unidirectional flow of aqueous anteriorly through the pupil, and the tight junctions of the iris epithelium, this pathway effectively shunts plasma-derived proteins and potential antigens toward the anterior chamber, thereby preventing their nonspecific diffusion into the posterior chamber.

The physiological consequences of this modified view of the blood–aqueous barrier are several. Given that the pathway shunts plasma-derived solutes unassociated with membrane transport mechanisms to the root of the iris, it is likely that a significant fraction of these solutes is almost immediately swept into the trabecular meshwork and aqueous outflow pathways. Recent studies have speculated that some of these solutes, such as added proteins, may represent a previously unrecognized contributor to normal aqueous outflow resistance, or even to the added resistance that elevates pressure in glaucoma.[10–13]

From clinical studies, there is evidence that subjects taking medications to suppress aqueous humor formation may demonstrate an increased plasma protein concentration in their anterior chambers.[14,15] Working from the previous model, the blood–aqueous barrier, the reasonable conclusion was that the drug produced a modest compromise in the blood–aqueous barrier integrity as an unwanted side effect. The present work offers an alternative explanation of the same data: it is equally likely that the increased concentration of protein results from the fact that the protein entry and aqueous production systems are not linked, as was previously assumed. Rather, as aqueous humor formation is decreased, the amount of fluid available to

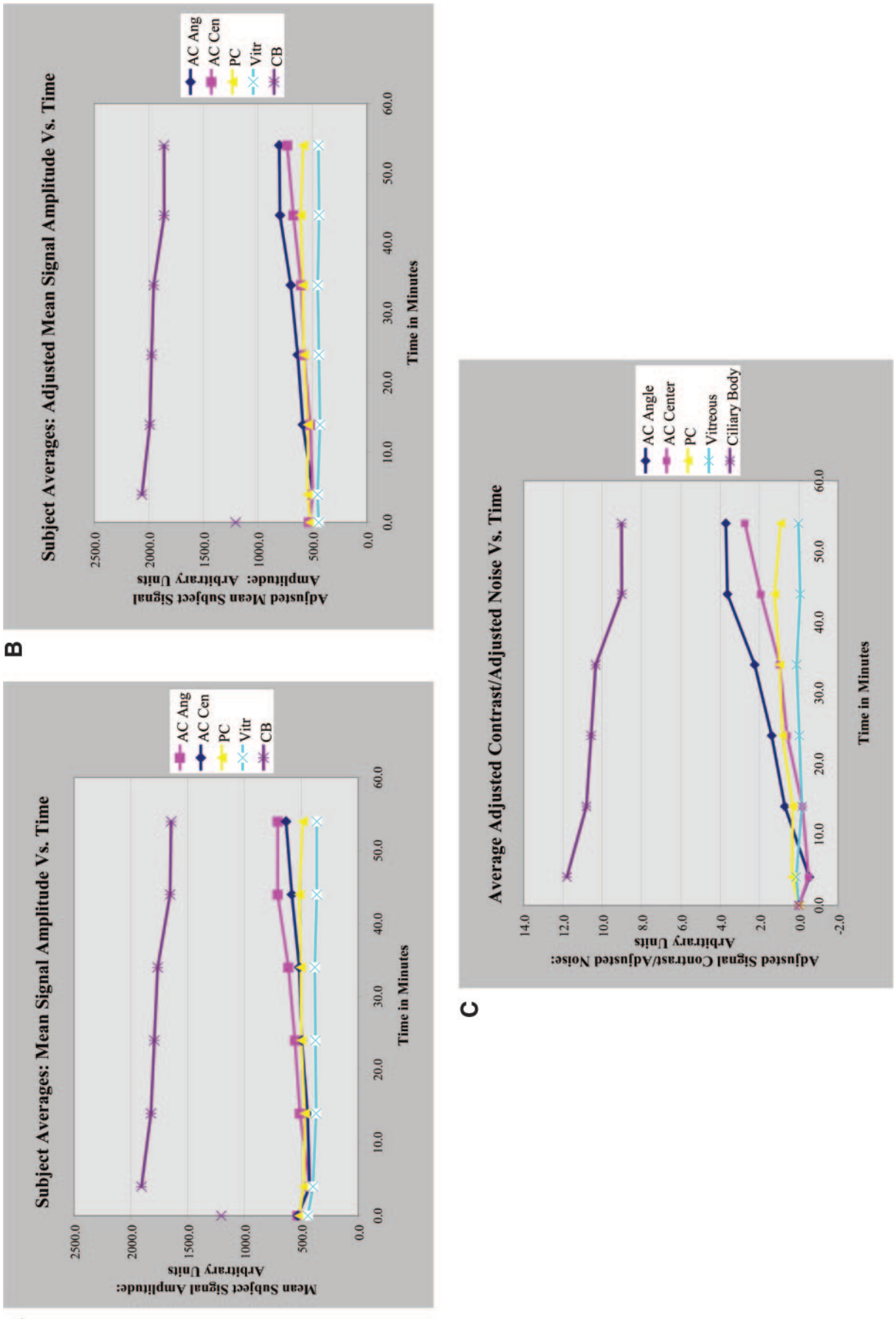

FIGURE 5. Scatterplots of composite data averaged (across all subjects at each time point) mean ROI signal amplitude, in arbitrary units versus time in minutes. (**A**) Mean signal averaged across all subjects versus time. (**B**) Adjusted mean signal averaged across all subjects versus time. (**C**) Adjusted contrast to adjusted noise ratios (*C/N*) versus time. Abbreviations are as in Figure 3.

TABLE 3. Probabilities Calculated by Wilcoxon Paired Tests for Comparisons of Maximum Enhancement within 60 Minutes

Enhancement vs.	Anterior Chamber Angle	Anterior Chamber Center	Posterior Chamber	Ciliary Body
Vitreous	0.0050	0.0050	0.0100	0.0050
PC	0.0100	0.0500	NA	0.0050
Noise	0.0050	0.0050	0.05	0.0050

Data are shown for comparisons between the anterior chamber angle, anterior chamber center, posterior chamber and ciliary body versus the vitreous and noise data, as well as comparisons between the anterior chamber angle, anterior angle center, and posterior chamber. Adjusted data, single tailed test.

dilute the continued shunting of solutes into the anterior chamber becomes less, and the protein concentration increases. This possibility has been previously considered,[15] but the postulate remains to be tested.

APPENDIX

The subsections of the Appendix are arranged to correspond with the references from the Methods section.

System Noise Analysis

The reconstruction of our images involved a standard procedure (i.e., a two-dimensional [2D] Fourier transform [FT]) followed by taking the magnitude of the complex voxel reconstructed signal intensity. Note that although the 2D FT is a linear transform that maintains the Gaussian probability distribution of the noise, the process of taking the magnitude converts this to a Rician distribution.[8,16,17] Furthermore, it is known that at high signal-to-noise ratios (SNRs), the Rician distribution becomes Gaussian. To measure the system white noise contribution, we therefore used a mathematical relationship that allows one to calculate the system white noise N_{sys} from the mean signal $\hat{S}_N$ in a background (noise only) region of the image: $\hat{S}_N = 1.253\ N_{sys}$.[8] $\hat{S}_N$ measurements were measured at each time point and then divided by 1.253 to correct for the Rician distribution. The data were then adjusted for autoscaling as described below and fit by linear regression to establish the time-dependent mean noise.

Autoscaling Corrections

An MRI scanner amplifies the signal it receives at several points while processing a signal. These amplification factors are typically set in a prescan procedure that first measures the signal and then adjusts the gain in various stages. Although important for clinical imaging, this autoscaling feature can result in erroneous results during experimentation, because a consistent gain is needed to compare images quantitatively from different data sets. In this Appendix, we first describe where autoscaling is applied to the data and then our approach to removing this autoscaling so that quantitative comparisons can be made between images acquired at different time points.

The analog portion of the receiver operates linearly as long as the amplitude of the signal does not exceed a certain value. Thus, one place where the amplification of the received signal is controlled is in the analog receiver, in order that the receiver is not saturated. Technically, the receiver for the time-dependent data is auto adjusted during a prescan procedure, so the maximum signal during the prescan is only a fraction of the signal that saturates the receiver (both analog and digital portions of the receiver). This insures that the operating point of the receiver is in a linear or unsaturated region. This autoscaling feature can result in erroneous readings during experimentation because, to compare image amplitudes from different data sets quantitatively, knowledge of changes in the scaling factor from image to image is needed (i.e., if the gain changes from one image to another, it changes the signal amplitude in a way that we must know for quantitative comparison of these different images). Therefore, we must know the ratio of the gains. In our case, we did not know this ratio from the scanner itself, but we estimated it by requiring the vitreous signal to remain constant. This is described later in the text in detail.

A second area where the data are sometimes autoscaled is in the reconstruction. Grayscale values for voxels in MRI are partitioned from a fixed range, a 16-bit word in the system used (Philips Medical Systems). Such a 12-bit word provides for 2^{12} or 4096 different grayscale levels. Air contains essentially no protons and is thus zero. The software usually sets the brightest objects in the field—typically fat in a T_1-weighted series—at some proportion (~70%) of the maximum value of 4096. The 4096 grayscale levels are then partitioned between these raw signals. Thus, if a perturbation produces a brighter object within the field during different study time points, a second autoscaling "gain" can alter the reconstruction. This can become apparent by changes in the SD of the noise signal and by changes in the intensity of objects that are not expected to change. Clinical MRI scanners are typically set to autoscale the reconstructed images. This feature, although very useful clinically (because it maintains a high dynamic range for the range of grayscale values in the image), will result in erroneous analyses when quantitatively comparing data from different image sets that have been scaled differently.

One might assume that one can correct for the changes in gain by requiring constant S/N_{sys} in structures that do not enhance with contrast. However, relative error can also occur because of truncation error in the noise (a phenomenon sometimes referred to as "binning") because of the relatively low absolute values of the pixels. Such errors become visible by systematic (rather than random) changes in S/N_{sys} in nonenhancing structures, such as the vitreous humor.

In addition, it is unavoidable that small changes in head and eye position occur in a set of scans performed over a 60- to 90-minute time period. Even such small changes can affect the signal obtained from thin (2-mm slice thickness), high-resolution (210–250-μm resolution in the plane of the slice) sections obtained with a surface coil that has inherent decrease in its sensitivity (and hence signal loss) with distance from the coil.

Because of these and other sources of both random and nonrandom variation, we used ROIs from nonenhancing structures to correct the data. We argue that the mean of the signal in these nonenhancing regions, in the reconstructed time-dependent images, should remain constant. Note that the signal in these nonenhancing structures is large enough to avoid the "binning" errors just discussed that are problematic when measuring the noise. We therefore applied a correction factor to the mean signal of each structure, based on maintaining a constant mean vitreous humor signal throughout the study. Note also that because the ROI for the vitreous humor was

large and contained a large number of voxels, the mean is very well determined.

We observed (Fig. 3A) a small decrease in the mean vitreous signal immediately after contrast administration. Thereafter, the vitreous signal changes linearly. This is consistent with the interpretation that the contrast agent, immediately after administration, causes an immediate increase in signal in some of the tissues (i.e., ciliary body and extraocular muscle) that makes the overall time-dependent input signal to the receiver larger. To compensate for this, the scanner may have reduced the receiver gain in the prescan setup to keep the maximum amplified signal constant.

We therefore studied correction factors to apply to the vitreous. We tested correction factors by fitting the data with test curves using the least-squares methods and evaluating the total sum of the squares of the errors occurring with a particular curve fit. Our best results were obtained by fitting the initial vitreous amplitude to a step function to account for the change in signal from baseline to the first data point after contrast administration, followed by a linear least-squares fit to the remaining data. This method consistently produced the least sum of the squared error for all test subjects (straight line and exponential curve fits were others that were tested). All time-dependent data were then corrected based on these fits to the vitreous time-dependent data (i.e., an initial step function followed by a linear correction applied to the postcontrast data). The step was equal to the mean signal of the vitreous precontrast data point minus the back-projected intercept of the linear least squares fit from all postcontrast data points. Note that $t = 0$ is defined as time of initiation of contrast administration, with the first postcontrast acquisition occurring at $t = 4$ minutes. The slope from the least-squares fit of the vitreous was then multiplied times the time variable and added to the step correction. This total correction was scaled to the precontrast ratio of the structure in question divided by the precontrast vitreous. The final equations for the correction factor are:

1. $\hat{S}_{sc}(0) = \hat{S}_{sm}(0)$, where $\hat{S}_s(0)$ represents the mean signal from an ROI within a structure taken from the baseline (nonenhanced) data set. The subscripts s, c, and m designate the structure of interest and the corrected and measured values. This simply states that the baseline, or unenhanced, images needed no correction.
2. $\hat{S}_{sc}(t) = \hat{S}_{sm}(t) + (\hat{S}_{sm}(0)/\hat{S}_{vm}(0))(\Delta\hat{S} - M \times t)$, where $\hat{S}_s(0)$ represents the mean signal from an ROI within a structure taken from the baseline (nonenhanced) data, $\hat{S}_s(t)$ represents the mean signal measured within an ROI from a structure at time (t) in minutes after contrast administration, and t is the actual value of time in minutes after administration of contrast. The subscripts m and c designate measured and corrected data. $\Delta\hat{S} = \hat{S}_{vm}(0) - B$. The subscript v specifically designates the vitreous humor (i.e., $\hat{S}_{vm}(0)$ is the precontrast measured data point for the vitreous humor). B is the $\hat{S}_v(t)$ intercept (back projection) predicted by the linear least-squares fit of vitreous data points of the curve calculated from $t = 4$ minutes (first postcontrast data point) to $t = 60+$ minutes (last postcontrast data point). M is the slope from the same curve fit.

Thus, autoscaling is dealt with by using these correction equations. In brief, a fit was made to the vitreous data. The deviation of this fit from the initial baseline value (i.e., $M \times t + B - \hat{S}_{vm}(0)$), is scaled by the ratio of the initial values of the structure in question to that of the vitreous. This gives the offset from the $t = 0$ value expected for the structure. This correction is subtracted from the measured value of the structure at time t to correct for autoscaling.

Contrast-to-Noise Calculations

$\hat{C}(t) = \hat{S}(t) - \hat{S}(0)$ where $\hat{C}(t)$ and $\hat{S}(t)$ represent mean ROI contrast (enhancement) and postcontrast mean ROI signal amplitude at time t. $\hat{S}(0)$ represents precontrast or baseline mean ROI signal ($t = 0$).

$\hat{C}_c(t)/N_c(t) = (\hat{S}_c(t) - \hat{S}(0))/N_c(t)$. Symbols and subscripts other than $N(t)$ are as previously defined. $N_c(t)$ represents the corrected mean noise at time t. The raw mean noise was fitted with its own correction function: a scaled step function plus linear fit of the postcontrast noise data, identical with the curve fit of the vitreous data. Final noise values were then corrected by the equations (1) $N_c(0) = N_m(0)$, where $N(0)$ designates precontrast mean ROI noise measurements and the subscripts c and m refer to corrected and measured values, respectively, which are identical for the baseline ($t = 0$) value and (2) $N_c(t) = (N_m(t) + \Delta N - M_n \times t)$, where: $N(t)$ designates mean ROI noise measurements at the post contrast time t, $\Delta N = (N_m(0) - B_n)$, and t is the recorded time after contrast. B_n and M_n are the back-projected intercept and slope from the least-squares fit of post contrast data points from $t = 4$ minutes (first postcontrast data point) to $t = 60+$ minute (last postcontrast data point). The subscripts c and m refer to corrected and measured values, respectively.

Logistic Curve

The parameters that were adjusted were the exponential constant k (exponential equivalent of slope) and the equilibrium value of the signal after contrast S_m (Table 2: For those unfamiliar with the logistic equation, it is an equation of the form: $\hat{S}(t) = S_i S_m/[S_i + (S_m - S_i)(e^{-kt})]$, where $\hat{S}(t)$ = the dependent variable [signal] at a given time point t [e.g., $\hat{S}(0)$, $\hat{S}(4)$ $\hat{S}(14)$; are signal precontrast, postcontrast at 4 minutes, postcontrast at 14 minutes], S_i is the initial value of the dependent variable [signal before enhancement], S_m is a fitted parameter for the equilibrium value of the dependent variable [equilibrium signal after contrast] and k is a fitted exponential parameter.)

References

1. Raviola. G. The structural basis of the blood-ocular barriers. *Exp Eye Res.* 1977;(suppl)25:27–64.
2. Freddo TF, Bartels SP, Barsotti MF, Kamm RD. The source of proteins in the aqueous humor of the normal rabbit. *Invest Ophthalmol Vis Sci*. 1990;31:125–137.
3. Barsotti MF, Bartels SP, Freddo TF, Kamm RD. The source of protein in the aqueous humor of the normal monkey eye. *Invest Ophthalmol Vis Sci*. 1992;33:581–595.
4. Freddo T. Aqueous humor proteins: a key for unlocking glaucoma? The 1992 Glenn Fry Award Lecture. *Optom Vis Sci*. 1993;70:263–270.
5. Kolodny N, Freddo T, Lawrence B, Suarez C, Bartels SP. Contrast-enhanced MRI confirmation of an anterior protein pathway in the normal rabbit eye. *Invest Ophthalmol Vis Sci*. 1996;37:1602–1607.
6. Erickson-Lamy K, Schroeder AM, Bassett-Chu S, Epstein DL. Absence of time-dependent facility increase ("washout") in the perfused, enucleated human eye. *Invest Ophthalmol Vis Sci*. 1990; 31:2384–2388.
7. Bert RJ, Patz S, Ossiani M, et al. High resolution MR imaging of the human eye. *AJNR Am J Neuroradiol Supplement.* 2006;13;368–378.
8. Haacke ME, Brown RW, Thompson MR, Venkatesan R. *Magnetic Resonance Imaging: Physical Principles and Sequence Design.* New York: Wiley-Liss; 1999:340.
9. Freddo, T. Intercellular junctions of the iris epithelia in Macaca mulatta. *Invest Ophthalmol Vis Sci.* 1984;25–1094-1104.
10. Johnson M, Gong H, Freddo TF, Ritter N, Kamm RD. Serum proteins and aqueous outflow resistance in bovine eyes. *Invest Ophthalmol Vis Sci*. 1993;34:3549–3557.

11. Sit AJ, Gong H, Ritter N, Freddo TF, Kamm RD, Johnson M. The role of soluble proteins in generating aqueous outflow resistance in the bovine and human eye. *Exp Eye Res*. 1997;64:813–821.
12. Russell P, Koretz J, Epstein DL. Is primary open angle glaucoma caused by small proteins? *Med Hypotheses*. 1993;41:455–458.
13. Doss EW, Ward KA, Koretz JF. Investigation of the "fines" hypothesis of primary open-angle glaucoma: the possible role of alpha-crystallin. *Ophthalmic Res*. 1998;30:142–156.
14. Stur M, Brabner G, Huber-Spitzy V, Schreiner J, Haddad R. Effect of Timolol on aqueous humor protein concentration in the human eye. *Arch Ophthalmol*. 1986;104:899–900.
15. Diestelhorst M, Roters S, Krieglstein GK. The effect of latanoprost 0.005% once daily versus 0.0015% twice daily on intraocular pressure and aqueous humour protein concentration in glaucoma subjects: a randomized, double-masked comparison with timolol 0.5%. *Graefes Arch Clin Exp Ophthalmol*. 1997; 235:20–26.
16. Haacke ME, Brown RW, Thompson MR, Venkatesan R. *Magnetic Resonance Imaging: Physical Principles and Sequence Design.* New York: Wiley-Liss; 1999:876.
17. Gudbjartsson H, Patz S. The Rician distribution of noisy MRI data. *Magn Reson Med*. 1995;34:910–914.

E R R A T U M

Erratum in: "Novel Mutations of *FOXC1* and *PITX2* in Patients with Axenfeld-Rieger Malformations" by Weisschuh et al. (*Invest Ophthalmol Vis Sci.* 2006;47:3846–3852).

The predicted Y115S missense change in *FOXC1* is caused by an A→C transversion at nucleotide position 334 (c.344A→C).